EQS Res-HBC: A 65-nm Electro-Quasistatic Resonant 5–240 μW Human Whole-Body Powering and 2.19 μW Communication SoC With Automatic Maximum Resonant Power Tracking

Nirmoy Modak, *Student Member, IEEE*, Debayan Das, *Member, IEEE*, Mayukh Nath, *Graduate Student Member, IEEE* , Baibhab Chatterjee, *Member, IEEE*, Gaurav Kumar K, *Student Member, IEEE*, Shovan Maity, *Member, IEEE*, and Shreyas Sen, *Senior Member, IEEE*

***Abstract*— Applications like connected healthcare through physiological signal monitoring and secure authentication using wearable keys can benefit greatly from the battery-less operation. Low-power communication along with energy harvesting is critical to sustain such perpetual battery-less operation. Human body channel is known to be a promising alternative to wireless radio wave communication for low power operation through human body communication (HBC), as well as very recently demonstrated as a medium for power transfer through body-coupled power transfer. However, channel length (L) dependency of the received power makes it inefficient for L>40 cm. In this article, we utilize electro-quasistatic resonant HBC (EQS Res-HBC) with maximum resonant power tracking (MRPT) to enable channel length-independent whole-body communication and powering. We design the first system to transfer power and data from a HUB device to wearable energy-harvested NODE through the human body to enable battery-less perpetual operation. Measurement results show 240, 28, and 5 μW power transfer through the body in a machine–machine (large devices with strong ground connection), tabletop (small devices kept on a table), and wearable–wearable (small form factor battery-operated wearable devices) scenario, respectively, independent of body channel length, while enabling communication at 2.19 μW. This enables >25× more power transfer with >100× more efficiency compared to the state of the art for 100-cm body channel in tabletop scenario by utilizing the benefits of EQS operation. The MRPT loop automatically tracks device and posture-dependent changes in the resonance point to maximize power transfer in all cases.**

***Index Terms*— Electro-quasistatic resonant human body communication (HBC) (EQS Res-HBC), low power, perpetual HBC operation, physiological monitoring, whole body powering.**

Manuscript received July 29, 2021; revised November 4, 2021; accepted December 29, 2021. Date of publication January 25, 2022; date of current version February 24, 2022. This article was approved by Associate Editor Farhana Sheikh. This work was supported in part by the Air Force Office of Scientific Research YIP Award under Grant FA9550-17-1-0450 and in part by the National Science Foundation (NSF) Career Award under Grant 1944602. *(Corresponding author: Nirmoy Modak.)*

This work involved human subjects or animals in its research. Approval of all ethical and experimental procedures and protocols was granted by the Purdue Institutional Review Board under IRB Protocol No. 1610018370.

The authors are with the Elmore Family School of Electrical and Computer Engineering, Purdue University, West Lafayette, IN 47907 USA (e-mail: nmodak@purdue.edu; shreyas@purdue.edu).

Color versions of one or more figures in this article are available at https://doi.org/10.1109/JSSC.2022.3142177.

Digital Object Identifier 10.1109/JSSC.2022.3142177

I. Introduction

IN APPLICATIONS like physiological signal monitoring and secure authentication, low data rate but extremely low-power secure communication is required around the human body. In recent years, human body communication (HBC) [1]–[5] has emerged as a power-efficient alternative to traditional wireless communication, such as Bluetooth, ANT, and Zigbee. Even though today's HBC transceivers offer low-loss and low power consumption, there is a strong need of making the entire operation battery-less and perpetual. Also, there have been a few studies for low-power communication through the human body, but none of them could provide sustainable battery-less operation except one of the works [6], which still relies on the ambient sources and is not efficient at long channel. Previous studies have used techniques such as Tribo-Electric, Piezo-Electric, and RF energy harvesting for Body Area Network devices, but they are restricted only to on-body node placement.

Power transmission using near field with inductive link suffers from alignment issues and it is limited to short distances. To alleviate the alignment issue, a self-localization method is used by placing the node under the eTextile shirts, but the position of the node receivers is still confined in this method [7]–[9]. RF-based power transmission experiences 40–60 dB loss in body area network for a body channel length of >40 cm, making the process inefficient for power transmission [10]–[13]. Some other types of conventional energy-harvesting techniques have also been utilized for powering purposes, but these are limited to the specific parts of the body [14]–[16]. For example, piezoelectric [14] and triboelectric [15] generators which can be categorized as electrostatic harvesters can only operate at joints and underfoot. Similarly, photovoltaics harvesting only be used in the sensors with conditional access to the direct sunlight [17]. Energy

harvesting from EM waves also needs correct body positioning to avoid the degradation in the efficiency induced by the body shadowing effect [18]. The most recent work [5] proposes the body-coupled power transmission and ambient energy harvesting utilizing human body-coupling to deliver power to the entire body, and at the same time harvesting energy from ambient EM waves coupled through the body. But this work is not suitable for long channel (60–100 cm) power delivery as the efficiency reduces less than 1%. Also, the power delivered to the body in this method is significantly high exceeding the limit set by [19], [20].

In this work, we utilize electro-quasistatic HBC for whole-body power transfer and data communication using the same IC. The electro-quasistatic operation allows whole-body power transfer without any efficiency degradation as channel length increases. We also utilized EQS resonant operation to increase the peak power delivered within a short interval of time with increased efficiency. The cancellation of device cap and return path capacitances are done by placing inductor coils at different parts of the channel which minimizes the communication power loss but at the same time maximizing the figure of merit (FoM) of the communication. Variations in the channel introduced by the movements of the body, different body postures, and surroundings are taken care of by a maximum resonant power tracking (MRPT) method which ensures correct resonance frequency during the power delivery and communication.

The key contributions of this proposed work are as follows:

1) The first implementation of electro-quasistatic resonant HBC (EQS Res-HBC) IC for whole body powering and data transfer through the human body.
2) The first bio-physical model of EQS Res-HBC for efficient powering and higher communication FoM.
3) Cancellation strategy of device capacitance for reduced power during communication.
4) A real-time MRPT, or MRPT loop and single sampler sensing scheme.
5) Demonstration of a battery-powered HUB for power delivery and an energy-harvested NODE for battery-less perpetual operation with an ON-chip clocking mechanism for self-sustained functioning.

The rest of this article is organized as follows: Section II discusses the theoretical concept behind the EQS resonant HBC for efficient power and communication through the human body using lumped element-based model. Section III discusses the detailed circuit-level architecture and design of the transmitter, receiver, resonance scanner, and energy harvester. Section IV discusses the various measurement results, power and data transfer demonstration, and comparison with the state of the arts. Section V concludes the work.

II. Electro-Quasistatic Resonant Human Body Communication: Theory

Low-power secure link is one of the key features of HBC. Conventional wireless body area networks (WBAN) such as Bluetooth suffers from high-power requirements and physical signal leakage. However, EQS-HBC utilizes the conductivity of the human body to use it as a communication medium and makes the communication protected by keeping the signal confined within close proximity of the body. Although countless works have been done to show the communication and powering between two wearable devices, the whole body power transfer in the wearable–wearable scenario is not demonstrated yet. AN FEM-based simulation as in Fig. 1 shows that EQS operation can deliver uniform power to the whole body, making the wearable–wearable power transfer a reality.

Fig. 2 shows an HBC transceiver system capacitively connected to the human body using a metallic dry electrode. The positive electrode of the transmitter and receiver are on the human body surface, while the negative electrodes are kept floating. The E-field lines are shown on the same figure to visualize the signal forward and return path. The E-field lines between the negative Tx electrode to the earth ground and the negative Rx electrode to the earth ground form $C_{\text{ret(TX)}}$ and $C_{\text{ret(RX)}}$, respectively; the E-field lines between the human body and the earth ground forms C_{Body}; the E-field lines between the parallel plates of the transmitter and receiver introduce the plate capacitor C_P at the transmitter side and C_L at the receiver side. In the EQS frequency (0.1–10 MHz) regime, all these lumped elements form the EQS-HBC bio-physical model as discussed in [1]. The parameters of the bio-physical model are constant in a static environment, but changes with movement and body posture. The contact resistance of the electrodes is neglected due to the lower impedance value of those electrodes compared to the impedance of the return path capacitances within EQS frequency regime.

A. EQS-HBC Circuit Model

An EQS-HBC bio-physical model with source resistance R_S and receiver resistance R_{RX} is shown in Fig. 3(a). The effective load to the transmitter is R_S+Z_C, where the effective impedance to the right side of R_S is represented as Z_C in the following:

$$Z_C = \frac{1}{sC_P + \frac{1}{\frac{1}{sC_{\text{ret}(TX)}} + \frac{1}{sC_{\text{Body}} + \frac{1}{\frac{1}{sC_{\text{ret(RX)}}} + \frac{1}{sC_L + \frac{1}{R_{\text{RX}}}}}}}}. \tag{1}$$

The electrode capacitances C_P and C_L are in the range of 10–30 pF. The return path capacitance $C_{\text{ret(TX)}}$ and $C_{\text{ret(RX)}}$ are <1 pF each, whereas the body capacitance C_{Body} is 100–200 pF. In the EQS frequency regime,

$$\left|\frac{1}{sC_{ret(RX)}}\right| \gg \left|\frac{1}{sC_L + \frac{1}{R_{RX}}}\right|$$
$$\left|\frac{1}{sC_{ret(TX)}}\right| \gg \left|\frac{1}{sC_{Body} + sC_{ret(RX)}}\right|$$

and $|sC_P| \gg |sC_{\text{ret(TX)}}|$. With all these approximations, the effective impedance Z_C can be approximated as $(1/sC_P)$. Therefore, the effective load to the transmitter can be written as

$$Z_{\text{LOAD(TX)}} = R_S + \frac{1}{sC_P}. \tag{2}$$

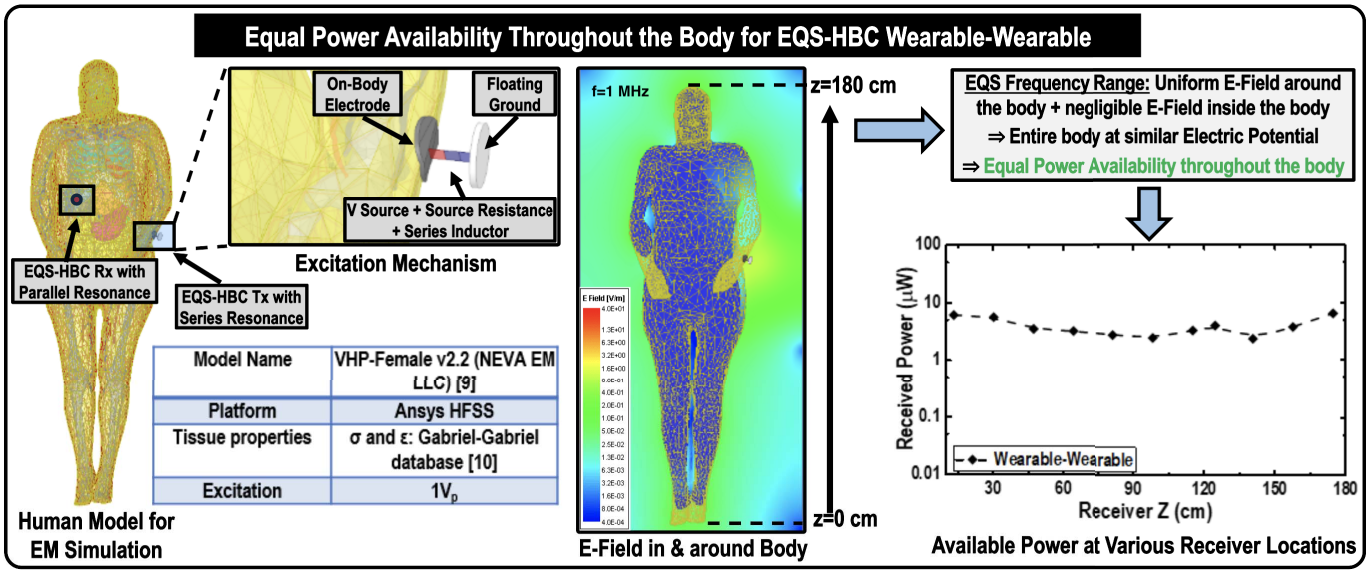

Fig. 1. FEM simulation showing power availability throughout the body during an EQS-HBC wearable–wearable power transfer.

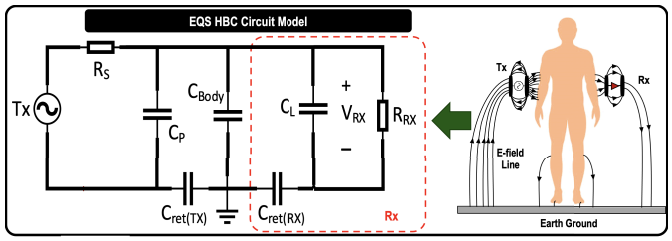

Fig. 2. Bio-physical model of electro-quasistatic capacitive HBC.

In voltage mode communication, neglecting the loading effect of the capacitors, the maximum received voltage can be expressed as

$$V_{\mathrm{RX_{max}}} = \frac{C_{\mathrm{ret(TX)}}}{C_{\mathrm{Body}}} \frac{C_{\mathrm{ret(RX)}}}{C_L} V_{\mathrm{TX}} \tag{3}$$

where we have considered $R_S \ll (1/sC_P)$ and $R_{\mathrm{RX}} \gg (1/sC_L)$ to get the maximum possible voltage transfer at the receiver side. During the power transfer, the transmitted power and the maximum power available at the receiver side with impedance matching is expressed by the following, respectively,

$$P_{\mathrm{TX}} = \frac{V_{\mathrm{TX}}^2}{2|Z_C|} \tag{4}$$

$$P_{\mathrm{RX_{max}}} = \frac{V_{\mathrm{RX_{max}}}^2}{8R_{\mathrm{RX}}}. \tag{5}$$

B. EQS Series Resonant HBC

As we can see from (5), the maximum power available to the receiver is proportional to the square of the peak-to-peak voltage $V_{\mathrm{RX_{max}}}$. Therefore, higher received power demands higher $V_{\mathrm{RX_{max}}}$. From (3), it is seen that $V_{\mathrm{RX_{max}}}$ is a function of C_{Body}, C_L, $C_{\mathrm{ret(TX)}}$, $C_{\mathrm{ret(RX)}}$, and transmitted voltage V_{TX}. Out of these four capacitances, we do not have control over $C_{\mathrm{ret(TX)}}$, $C_{\mathrm{ret(RX)}}$, and C_{Body}. However, the load capacitance C_L has a minimum limiting value due to the device size restriction. Therefore, the increase in $V_{\mathrm{RX_{max}}}$ can only be done by increasing the transmitted voltage V_{TX}. In sub-micrometer CMOS technology, the supply voltage itself has an upper limit which puts limitation on the maximum power transfer by limiting the peak transmitted voltage. To overcome this restriction without exceeding the supply limit, the transmitted voltage is increased by series resonance at the transmitter end. Series resonance increases the voltage across C_P by a factor Q and the available power to the receiver by a factor Q^2 at resonance. A parallel inductor at the receiver end increases the received voltage further by a factor Q, making the overall power increment by a factor Q^4 at resonance frequency. The bio-physical circuit model of EQS series resonant HBC is shown in Fig. 3(b). At resonance frequency, due to the inductive cancellation, the effective load seen by the transmitter is given by the following:

$$Z_{\mathrm{LOAD(TX)}} = R_S + R_L \approx R_L \tag{6}$$

where the inductor resistance R_L is considered much higher compared to the source resistance R_S. The transmitted power, received voltage, and maximum received power at resonance frequency are given by the following:

$$P_{\mathrm{TX}} = \frac{V_{\mathrm{TX}}^2}{R_L} \tag{7}$$

$$V_{\mathrm{RX}} = Q^2 \frac{C_{\mathrm{ret(TX)}}}{C_{\mathrm{Body}}} V_{\mathrm{TX}} \tag{8}$$

$$P_{\mathrm{RX_{max}}} = \frac{Q^4}{8R_{\mathrm{RX}}} \left[\frac{C_{\mathrm{ret(TX)}}}{C_{\mathrm{Body}}} V_{\mathrm{TX}} \right]^2. \tag{9}$$

C. EQS Parallel Resonant HBC

The efficiency of a voltage mode communication is defined by the figure of merit (FoM) which is the ratio of the received voltage V_{RX} to the transmitted power P_{TX}. Series resonance

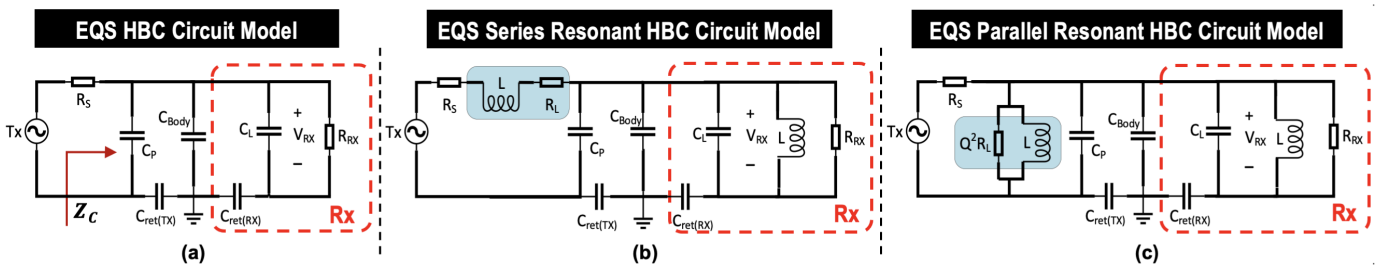

Fig. 3. Different types of EQS HBC models. (a) Regular EQS HBC model showing transmitter and receiver. (b) EQS series resonant HBC with a series inductor at the transmitter and a parallel inductor at the receiver end. (c) EQS parallel resonant HBC with a parallel inductor at the transmitter and another parallel inductor at the receiver end.

helps increase the peak transferred power using inductive cancellation at the transmitter end. But, this technique cannot reduce the power loss on the parallel plate capacitor C_P. To attain higher FoM during the voltage mode communication, reduction of the power loss at the transmitter end is highly recommended. The wasted power on the parallel plate capacitor C_P can be reduced by placing an inductor parallel to C_P. Parallel resonance reduces the transmitter current by a factor Q at resonance without altering the transmitted voltage which decreases the overall power consumption by a factor Q^2, that is, Q^2 times increase in FoM. At the receiver side, another parallel inductor increases the received voltage by a factor Q making the overall FoM Q^3 times more than the regular EQS HBC. The bio-physical circuit model of EQS parallel resonant HBC is shown in Fig. 3(c). At resonance frequency, due to the inductive cancellation, the effective load seen by the transmitter is given by the following:

$$Z_{\mathrm{LOAD(TX)}} = R_S + Q^2 R_L \approx Q^2 R_L. \tag{10}$$

The transmitted power, received voltage, and received power at resonance frequency are given by the following:

$$P_{\mathrm{TX}} = \frac{V_{\mathrm{TX}}^2}{Q^2 R_L} \tag{11}$$

$$V_{\mathrm{RX}} = Q \frac{C_{\mathrm{ret(TX)}}}{C_{\mathrm{Body}}} V_{\mathrm{TX}} \tag{12}$$

$$P_{\mathrm{RX_{max}}} = \frac{Q^2}{8 R_{\mathrm{RX}}} \left[\frac{C_{\mathrm{ret(TX)}}}{C_{\mathrm{Body}}} V_{\mathrm{TX}} \right]^2. \tag{13}$$

D. Comparison Between the HBC Models

A comparison table of three different EQS HBC models is shown in Fig. 4. The maximum peak power transfer is lowest in a regular EQS HBC and highest in the EQS series resonant HBC. The received power is Q^2 times more in series configuration compared to the EQS parallel resonant. On the other hand, FoM of the voltage mode communication increases significantly in both the resonance configurations. But the FoM in parallel resonant configuration is Q times more compared to the series resonant. Therefore, EQS series resonant HBC is the best choice for peak power transfer and EQS parallel resonant HBC is the best option for voltage mode communication. The condition for the transmitter or driver resistance is also mentioned in the table. In the series resonant configuration, we need source resistance R_S much lower compared to the

HBC Model	Maximum Peak Power Transfer ($P_{RX_{max}}$)	FoM for Voltage Mode Communication ($\frac{V_{RXmax}}{P_{TX}}$)	Driver Resistance (R_S)
EQS HBC	$\frac{1}{8R_{RX}}\left[\frac{C_{ret(TX)}}{C_{Body}}\frac{C_{ret(RX)}}{C_L}V_{TX}\right]^2$	$\frac{\lvert Z_C\rvert}{V_{TX}}\frac{C_{ret(TX)}}{C_{Body}}\frac{C_{ret(RX)}}{C_L}$	--------
Series Resonant HBC	$\frac{Q^4}{8R_{RX}}\left[\frac{C_{ret(TX)}}{C_{Body}}V_{TX}\right]^2$	$Q^2\frac{R_L}{V_{TX}}\frac{C_{ret(TX)}}{C_{Body}}$	$R_S \ll R_L$
Parallel Resonant HBC	$\frac{Q^2}{8R_{RX}}\left[\frac{C_{ret(TX)}}{C_{Body}}V_{TX}\right]^2$	$Q^3\frac{R_L}{V_{TX}}\frac{C_{ret(TX)}}{C_{Body}}$	$R_S \ll Q^2 R_L$

Fig. 4. Comparative study between EQS, EQS series resonant, and EQS parallel resonant HBC showing the maximum peak power transfer, FoM for voltage model communication, and condition for driver resistance.

equivalent inductor resistance R_L. A source with lower R_S ensures higher current during the resonance and increased power delivery to the receiver. Whereas in parallel resonant configuration, the driver resistance R_S has to be lower than $Q^2 R_L$ as shown in (10). At parallel resonance frequency, the current delivered by the transmitter is minimum which relaxes the condition for the source resistance R_S and a weaker driver can be used in parallel resonant HBC compared to the driver used in series resonant HBC.

E. Dependency of Resonance Frequency

In both the series and parallel resonant HBC, the resonance frequency is highly sensitive to the multiple model parameters. Using the equivalent circuit model, the resonance frequency can be determined by the following:

$$f_r = \frac{1}{\sqrt{L\left(C_P + \frac{C^*_{\mathrm{Body}} C_{\mathrm{ret(TX)}}}{C^*_{\mathrm{Body}} + C_{\mathrm{ret(TX)}}}\right)}} \tag{14}$$

where $C^*_{\mathrm{Body}} = C_{\mathrm{Body}} + (C_L C_{\mathrm{ret(RX)}}/C_L + C_{\mathrm{ret(RX)}})$. Load capacitance $C_L (\sim 10 - 30$ pF) is larger than the return path capacitance $C_{\mathrm{ret(RX)}} (\sim 0.5$ pF). Therefore, $C^*_{\mathrm{Body}} \approx C_{\mathrm{Body}} + C_{\mathrm{ret(RX)}} \approx C_{\mathrm{Body}}$ as C_{Body} ranges 100–200 pF which significantly higher than $C_{\mathrm{ret(RX)}}$. Considering these approximations, (14) can be rewritten as

$$f_r \approx \frac{1}{\sqrt{L\left(C_P + \frac{C_{\mathrm{Body}} C_{\mathrm{ret(TX)}}}{C_{\mathrm{Body}} + C_{\mathrm{ret(TX)}}}\right)}} \approx \frac{1}{\sqrt{L\left(C_P + C_{\mathrm{ret(TX)}}\right)}} \tag{15}$$

where $(C_{\mathrm{Body}} C_{\mathrm{ret(TX)}}/C_{\mathrm{Body}} + C_{\mathrm{ret(TX)}}) \approx C_{\mathrm{ret(TX)}}$ as C_{Body} is larger than the return path capacitance $C_{\mathrm{ret(TX)}} (\sim 0.5$ pF).

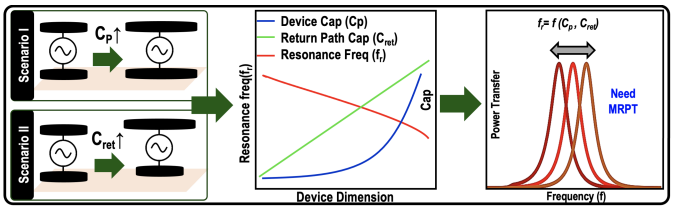

Fig. 5. Dependencies of resonance frequency on parallel plate capacitor C_P and return path capacitance C_{ret}.

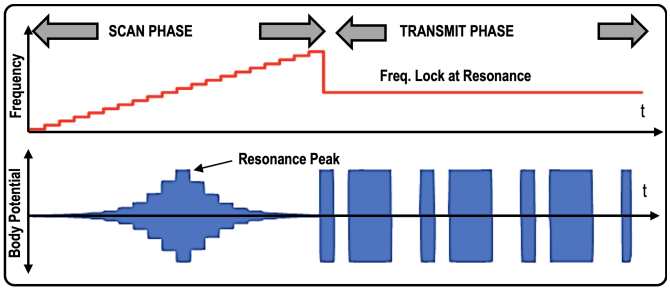

Fig. 6. Demonstration of HBC operation using scan phase for resonance detection followed by transmission at resonance frequency.

From (15), it is seen that the resonance frequency is mostly determined by C_P and $C_{\text{ret(TX)}}$ as shown in Fig. 5.

1) Dependency of Resonance Frequency on C_P: The parallel plate capacitance C_P mainly determines the frequency of the resonance. For a particular device with a fixed plate to plate distance, the device cap increases quadratically with the device radius. Scenario I in Fig. 5 shows as the device dimension increases, the capacitance C_P increases, and the resonance frequency falls.

2) Dependency of Resonance Frequency on $C_{ret(TX)}$: The return path capacitance $C_{\text{ret(TX)}}$ also contributes to determine the resonance frequency but the effect of $C_{\text{ret(TX)}}$ on resonance frequency is significantly low compared to the effect of C_P. According to the study [21], the value of the return path capacitance is linearly proportional to the radius of the floating electrode. Depending on the position of the transmitter on the body, the return path capacitance changes due to the body shadowing effect as described in [22]. In general, for a particular location on the body, as device dimension increases, the return path capacitance increases and resonance frequency falls as shown in Fig. 5 in Scenario II.

F. Maximum Resonant Power Tracking

The dependency of f_r on C_P is mostly time-invariant as C_P does not change once the particular device is made. But device-to-device variation may change the value of f_r across devices. A similar thing happens in the case of return path capacitance $C_{\text{ret(TX)}}$. f_r changes every time a person moves, as $C_{\text{ret(TX)}}$ is highly dependent on body posture, body shadowing effect, the position of the nearest earth ground, and size of the earth ground. Therefore, real-time on the go resonance frequency tracking is highly recommended for better operation. Fig. 6 shows the MRPT mechanism. The entire frequency tracking process is divided into two operations. In series resonance mode, a dedicated frequency scan phase changes the frequency from a lower limit to an upper limit in small discrete steps and records the peak body potential for each of the frequencies. During this process, the body potential attains the maximum value at the resonance frequency. Using this voltage peak information, the resonance frequency is detected at the end of the scan phase and the transmission phase begins at f_r.

III. System Architecture and Design

The overall proposed resonant HBC system architecture with futuristic internet of body (IoB [23]) vision is shown in Fig. 7. The full system has two different components: 1) a battery-operated HUB; 2) a battery-less NODE. A small Li-Po battery inside the HUB is the main source of power. A control unit in HUB runs the system in three different phases. 1) ϕ_1 phase: Transfers power to the NODE using series resonance. 2) ϕ_2 phase: Transfers DATA to the NODE using parallel resonance. 3) ϕ_3 phase: Receives the incoming DATA from NODE. The NODE unit also operates in sync with the HUB in three different phases. 1) ϕ_1 phase: Receives the incoming power using an energy harvester circuit and store it for future use. 2) ϕ_2 phase: Receives the incoming DATA from HUB. 3) ϕ_3 phase: Transfers DATA using parallel resonance. The synchronization among the three operational phases is done by a timer at the HUB and a finite state machine (FSM) at the NODE.

The power transfer and DATA communication need resonance detection for higher efficiency and FoM, respectively. The resonance frequency detection is done using a frequency scan cycle in HUB and after that, the powering or communication cycle begins. Therefore, the power transfer and data transfer are following the TDMA scheme. Simultaneous power and data transfer can also be done using a double resonance scheme with additional power budget but it is beyond the scope of this work. To save the power budget, the NODE frequency is kept in sync with the HUB Tx frequency. The frequency scan followed by powering or communication cycles are controlled by a digitally synthesizable control unit in HUB. The block-level architecture of the HUB and NODE is shown in Fig. 8. The circuit-level discussion of each of the individual blocks is given below in detail.

A. Synthesizable HUB Control Unit

The HUB control unit generates the required signal for HUB-NODE powering and communication. The HUB controller requires a READY signal generated from an external microcontroller or any other timing circuitry to initiate the operation. Once the controller receives the READY signal, it puts the HUB in a frequency scan cycle for resonance detection. An ON-chip digitally controlled oscillator generates the scan frequencies from a lower limit to an upper limit in discrete steps. Each scan frequency signal is exerted to the body through a series inductor and the body potential is measured. A feedback mechanism passes the body potential information to the control unit for reference. At the end of the scan cycle, the logic circuit in control unit decides the correct

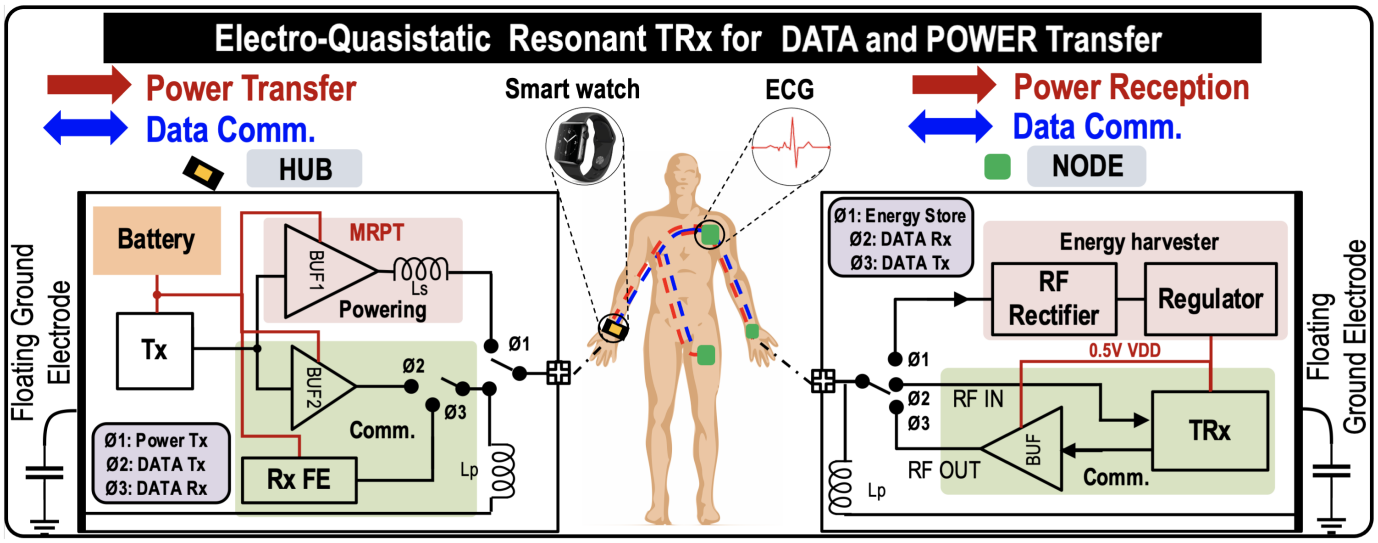

Fig. 7. Proposed block level architecture of the electro-quasistatic resonant HBC transceiver system. A battery-operated HUB unit operates in three different phases to interact with a battery-less NODE unit which operates in sync with the HUB for power reception, data reception, and data transmission.

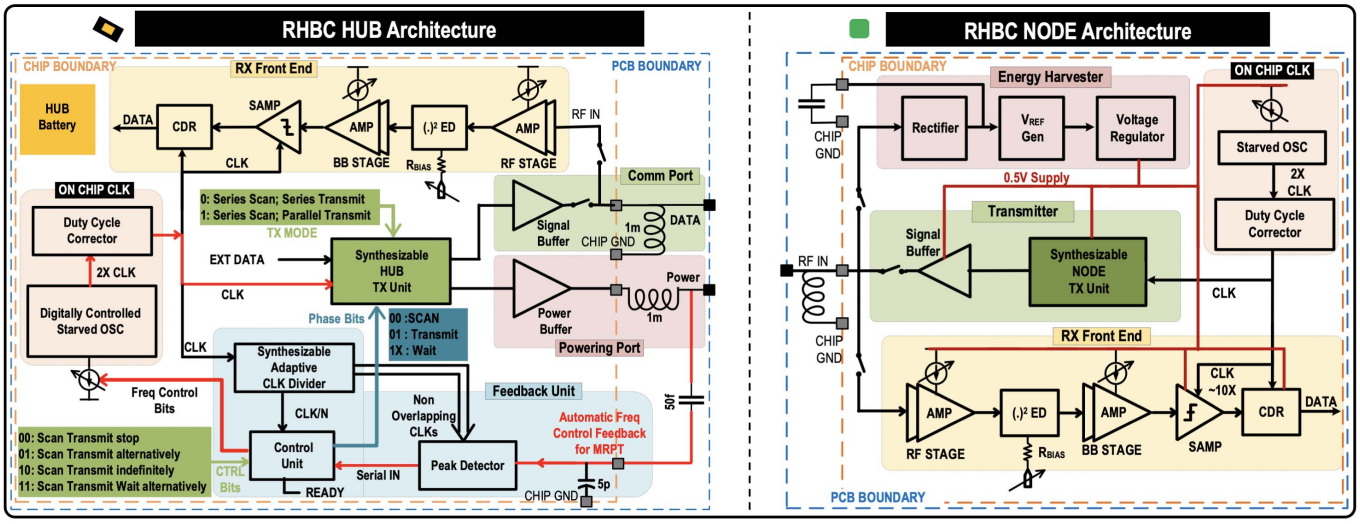

Fig. 8. Detailed architectural block diagram of the EQS resonant HBC HUB and NODE.

resonance frequency to initiate the power or DATA transmission cycle at resonance. A user-defined configurable register bit in the controller sets the resolution of the scan frequencies, upper and lower limit of the scan frequencies, duration of the transmission phase, and the number of repetition of the entire process with or without wait (or ideal) state.

B. ON-*Chip Clock Generator*

A low-power energy-efficient HBC system demands an ultralow power ON-chip clocking. A simple technique for ON-chip clock generation should be a ring oscillator as shown in Fig. 9. A three-stage current starved ring oscillator is used to generate the desired clock frequencies. The bias current of each of the starved inverters is controlled digitally using a 6-bit digital signal. The output of the ring oscillator is first passed through a two-stage amplifier designed using self-bias inverters. Amplification of the oscillator output ensures rail-to-rail clock signal swing. Then the amplified clock signal is further passed through a duty cycle corrector circuit which ensures the output clock with 50% duty at half of the oscillator frequency. The duty cycle corrector is designed using an XOR gate followed by a D-flip-flop in the feedback path. The oscillator produces 100 kHz to 3 MHz clock at 0.5-V supply voltage and 100 kHz to 5.1-MHz clock at 0.6-V supply voltage using the 6-bit digital code. During the frequency scan cycle, the HUB control unit changes the oscillator frequency in discrete steps to find the resonance frequency of the HBC channel. After the resonance detection, the oscillator frequency is locked and the entire system operates at resonance.

C. Fully Synthesizable Transmitter

The fully synthesizable transmitter is shown in Fig. 10. The transmitted data can be loaded from an external data source or can be generated from a programmable PRBS

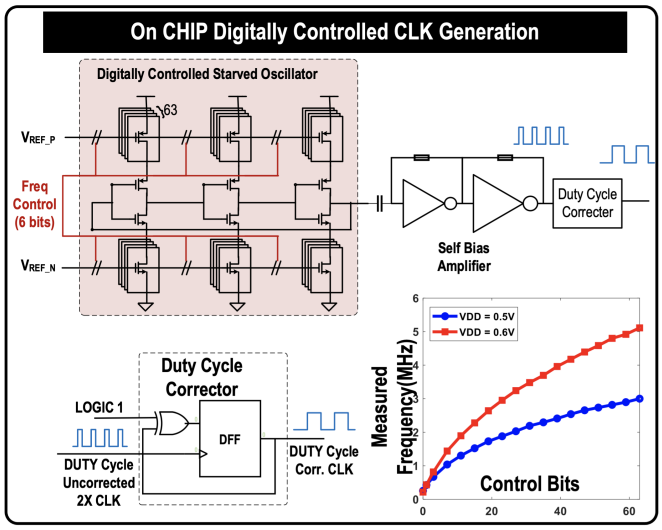

Fig. 9. ON-chip 6-bit digitally controlled starved ring oscillator-based clock generator with the duty cycle corrector.

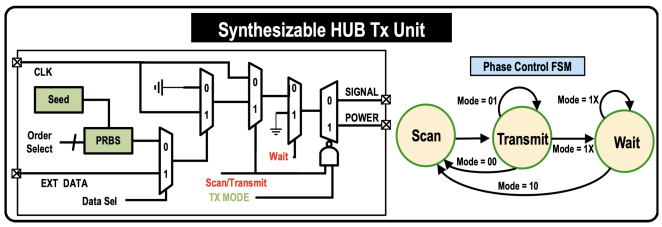

Fig. 10. Digitally synthesizable HBC HUB transmitter with phase control FSM.

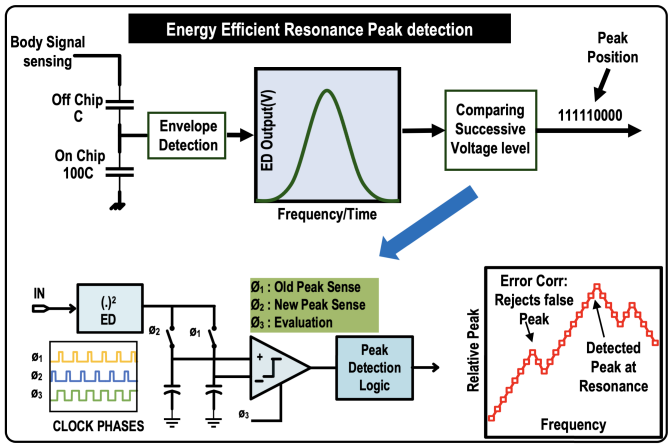

Fig. 11. Resonance sensing circuitry consisting of a capacitive voltage divider followed by an ED and successive voltage-level comparator.

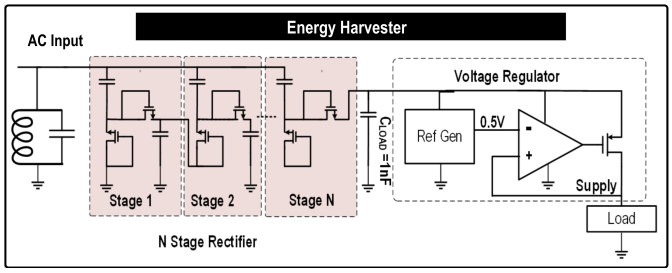

Fig. 12. Energy harvester showing a N-stage rectifier, OFF-chip capacitor, and reference generator followed by a supply generator.

generator. OOK modulation is chosen for simple modulation/demodulation circuit implementation while maintaining a very low power budget. The modulation is done using Direct Digital Synthesis (DDS) by passing the carrier clock through a multiplexer with the baseband data connected to the select line of the multiplexer. The ON-chip clock is used as a carrier for communication, and the baseband data is generated by dividing the carrier clock.

The signal port and the power port are the two output ports of the transmitter. The signal port is used during DATA communication which takes the advantage of parallel resonance for ultralow power communication and the power port is used during the power transfer which takes the advantage of the series resonance for maximum peak power transfer within a short interval of time. The three "Scan," "Transmit," and "Wait" transmitter modes are fully user-defined and digitally configurable which can be controlled by the control unit present in the HUB system.

D. Communication and Powering Buffers

In Section III, we have discussed the series and parallel resonances and the condition for the buffer/driver impedance. The requirement for powering and data communication are $R_S \ll R_L$ and $R_S \ll Q^2 R_L$, respectively. The driver circuity generally consumes 90% of the total power as it drives the body. Therefore, the designing of the driver buffers demand very careful attention. A weak buffer is incapable of driving the body capacitance with peak-to-peak potential. A strong buffer consumes a lot of unnecessary power due to the rise in leakage current. The powering buffer and communication buffer are implemented using a chain of six and four inverters, respectively. The first inverter of each of the chains is implemented with a minimum size inverter $((W_n/L_n) = (120\ \text{nm}/60\ \text{nm}))$ followed by $4\times$ increment in driving capability in each of the succeeding stages.

E. Feedback Unit

The feedback unit in the HUB system is one of the most crucial blocks. It helps determine the correct resonance frequency by feeding back the body potential information into the IC. The resonance sensing and feedback process start with a capacitive divider network as shown in Fig. 11 (also in Fig. 8). During the frequency scan cycle, due to the series resonance action, the body potential reaches peak value at resonance frequency. This potential cannot be sent back to the IC directly for sensing, as the scan frequency approaches toward resonance, the potential of the body may reach up to tenth of volt which may lead to voltage breakdown. Therefore, attenuation of the body potential before feeding back to the IC is necessary. A capacitive voltage divider network is implemented using a combination of an ON-chip and an OFF-chip capacitors for attenuation of the body potential. A 5-pF ON-chip capacitor with a 50 fF (or 100 fF)

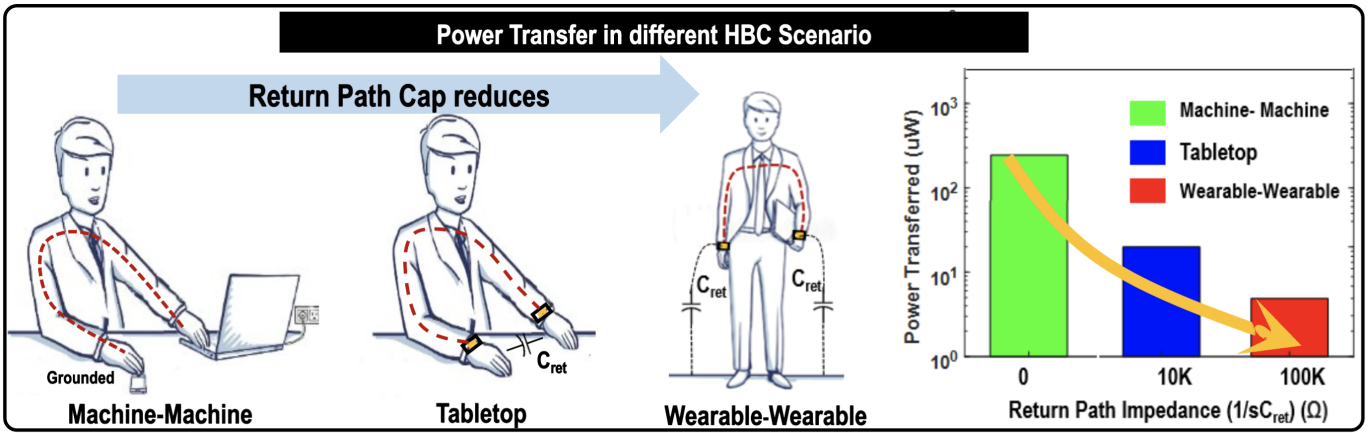

Fig. 13. Power transfer in three different HBC scenarios showing the dependency of transferred power on return path impedance.

OFF-chip capacitor is used to attenuate the signal by 100× (or 50×). Attenuation of the signal using an OFF-chip capacitor ensures peak signal value not exceeding by 100 mV to the IC pin. This voltage signal is then passed through a four-stage gate biased ED as mentioned in [24]. By controlling the bias voltage to the gate of the ED transistors settling time less than 40 μs is achieved while keeping 18 dB ripple rejection. Due to the square law, the ED output reaches significantly high at resonance frequency. As the scan frequency changes from the lower frequency limit to the resonance frequency, the output of the ED increases and attains the maximum value at a frequency that is closest to the resonance. Above the resonance frequency, a further increase in the scan frequency reduces the output of the ED as the frequencies are moving away from the resonance. A successive voltage-level comparator compares the voltage information of ED output for two consecutive scan frequencies. A strong-arm latch-based dynamic comparator with residual noise and offset less than 1 mV is used [25]. A capacitive sample and hold network with nonoverlapping clocks are used to hold the ED output for consecutive scan frequencies to store the old and new voltage peak information. The comparator generates logic high at the end of each comparison till the resonance frequency is reached, and after that, it generates logic lows. The comparator-generated serial output is feed to the control unit in the HUB and the resonance peak information is extracted. This single sampler sensing scheme makes the resonance detection more energy efficient than any other ADC-based sensing. The resonance detection logic is also made robust enough so that it rejects any false peak glitches.

F. Synthesizable Adaptive Clock Divider

Power management in the HBC TRx system is very critical for long-lasting operation. The transmitter unit in the proposed HUB system does data and power transfer at resonance frequency and the frequency is generated by the ON-chip oscillator. Except these two blocks, all the other auxiliary components in the HUB can be operated at 100–1000× lower frequency to reduce the power budget. A synthesizable adaptive clock divider unit is included in the design for proper frequency management as shown in Fig. 8. During the scan cycle, the control unit keeps on changing the oscillator frequency for resonance detection. If we transmit the scan frequency for an equal cycle count, the time duration for each of the scan frequencies decreases as frequency increases. This creates a settling issue of the ED output present in the feedback loop. Linear increment of the cycle count as scan frequency increases ensures equal time duration to each of the scan frequencies. The adaptive clock divider also generates three non-overlapping clocks required for resonance peak detection in the feedback loop as shown in Fig. 11.

G. Energy Harvester

The HBC NODE employs a 30-stage energy harvester circuit which utilizes the sub-threshold dicks on multiplier topology [26] to convert the received ac power from the HUB to a dc voltage as shown in Fig. 12. Since the transmitted voltage during power transfer from the HUB goes through ~60 dB channel loss though the human body [1], the received signal is in the range of 10s of mV. To have enough dc signal, 30 stages are employed in the energy harvester, which utilizes zero threshold voltage transistors to build up 1-V dc output at a 40 μF OFF-chip output capacitor. The sensitivity of the harvesting module is about 70-mV peak-to-peak. The length of the transistors is optimized for lower leakage. From measurements, the external capacitor takes 14 s to charge initially to 1 V. Since the communication module consumes ~2 μW, the 40-μF capacitor can support at least 10 s of data transmission before the storage capacitor voltage reduces to 0.5 V (below which the LDO's output does not remain fixed at 400 mV). This warrants a duty-cycled operation at the NODE. For example, powering for 15 s and communicating for 5 s works well for the current implementation.

H. HUB and NODE Receiver

The EQS resonant HBC receiver in HUB and NODE have identical circuit blocks. It consists of an analog front end (AFE), envelop detector (ED), baseband amplifier, sampler, and an over-sampling CDR. The AFE is a two-stage current

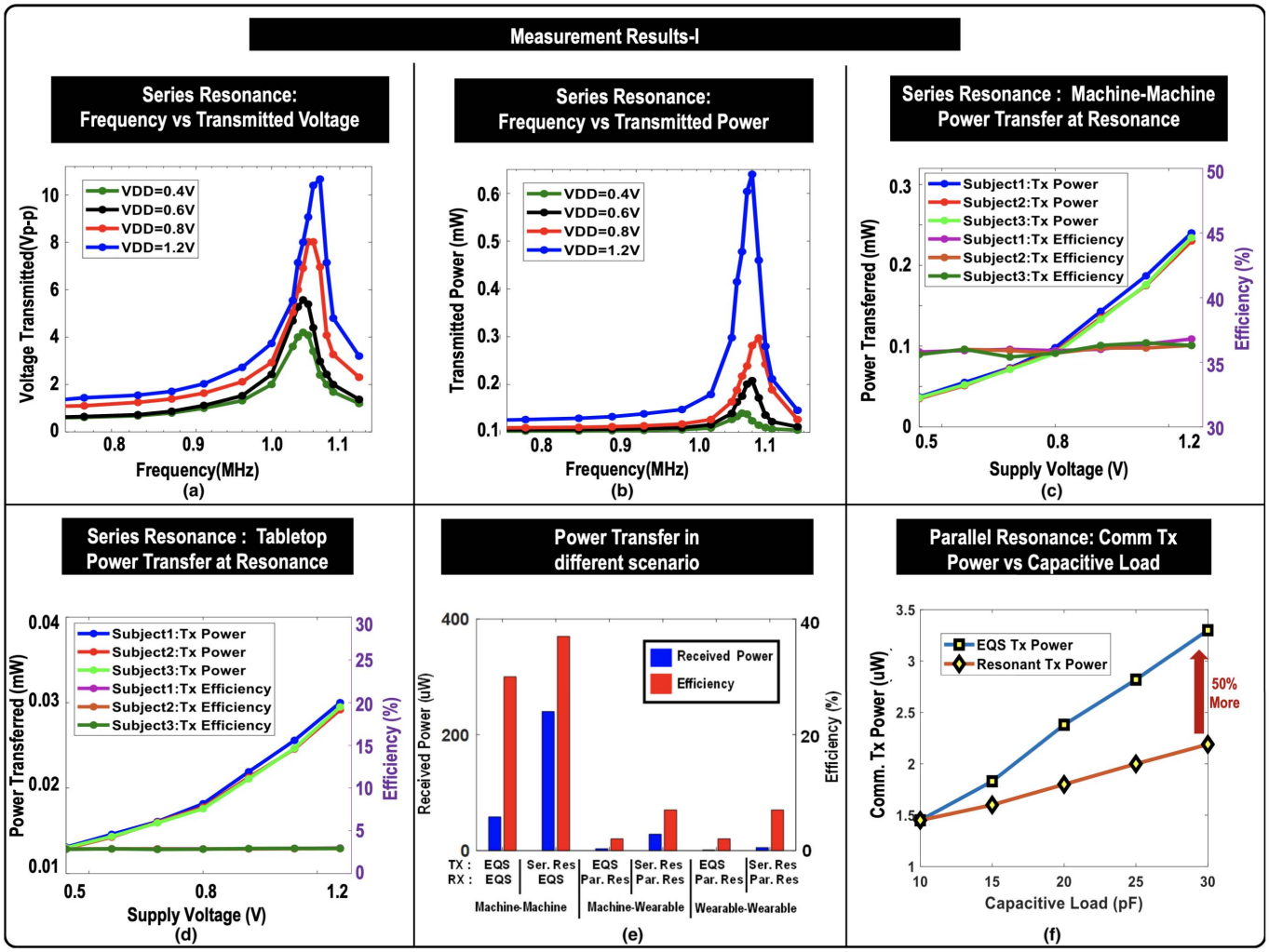

Fig. 14. Measurement results of the EQS resonant HBC HUB performance. (a) Peak-to-peak transmitted voltage with respect to frequency at different supply voltage during machine–machine interaction. (b) Transmitted power with respect to frequency at different supply voltage during machine–machine interaction. (c) Machine–machine power transfer and efficiency on three different subjects at resonance frequency in different supply voltage. (d) Power transfer and efficiency on three different subjects at resonance frequency in different supply voltage during tabletop HBC scenario. (e) Comparative plot of power transfer and power transfer efficiency in different HBC scenario. (f) Comparative plot of transmitter power versus capacitive load during data communication showing the improvement of EQS parallel resonant HBC over EQS HBC.

starved drain feedback common source amplifier [4]. A tunable gate bias ED demodulates the received signal [27], followed by a baseband amplifier for further amplification. The baseband data is sampled using a strong-arm latch-based sampler at $\sim$100$\times$ higher frequency to obtain rail-to-rail baseband data. Both the HUB and Node receivers are equipped with a fully synthesized oversampled clock and data recovery (CDR) unit. The oversampled clock rate for the CDR is configurable in the range 50 kbps–1 Mbps, which is at least 50$\times$ higher than the data rate supported. A finite state machine (FSM) within the CDR determines the minimum number of oversampled clock periods within the zero-phases or one-phases of the data, to find out the sampling clock duration. The sampling clock period dynamically adapts to the minimum data phase (one or zero). However, a clock jitter corrector logic ensures that the sampling clock period is not changed due to any random jitter in the minimum data phase. Similarly, a glitch corrector logic ensures that the FSM does not respond to unexpected data glitches to set an unreasonably high sampling clock frequency.

IV. Measurement Results

The EQS resonant HBC HUB and NODE are fabricated in TSMC 65-nm LP CMOS technology and have an active area of 0.13 mm^2 in total. We have measured the transmitted voltage, transmitted power, and power transfer efficiency in different frequencies. We also compare the power transfer values for three completely different HBC scenarios (machine–machine, tabletop, or wearable–wearable) as shown in Fig. 13. Return path capacitance changes significantly as shown in [21], depending on the scenario which changes the measurement results drastically. Therefore, the measurement data, specifically mentioning these three cases, is highly recommended.

A. Power Transfer

The power transfer profile such as transmitted voltage (V_{TX}), transmitted power (P_{TX}), received power (P_{RX}), and power transfer efficiency (η) are shown as a function of HUB Tx supply voltage at different frequencies for machine–machine

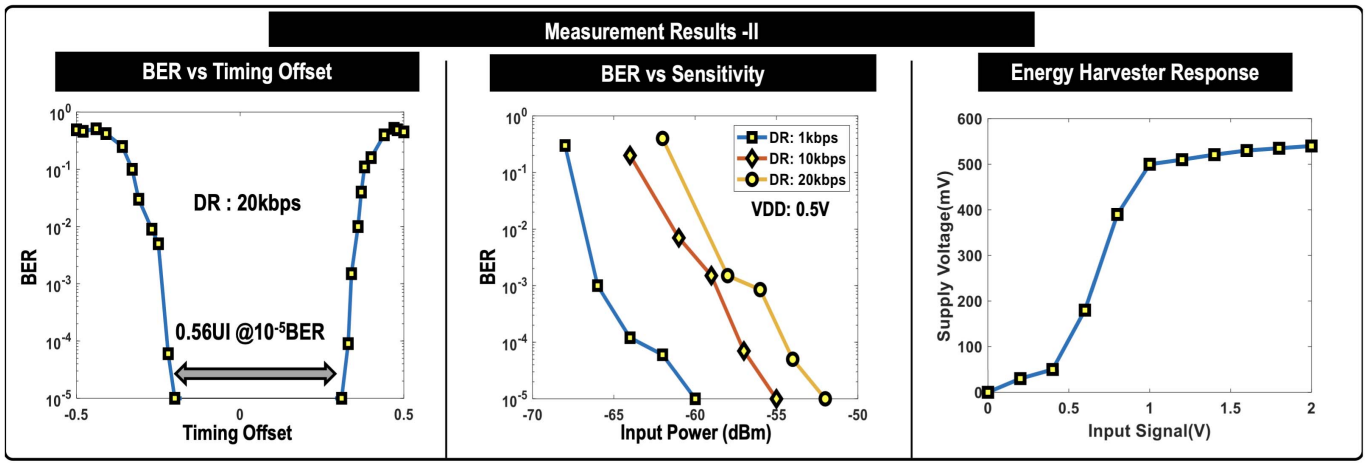

Fig. 15. Measurement results from the EQS resonant HBC receiver performance. (a) Bathtub curve of the receiver at 20-kbps data rate showing 0.56 UI opening at 10^{-5} BER. (b) Sensitivity analysis of the receiver showing −68-dBm sensitivity with 1-kbps data rate at the highest sensitivity point. (c) Plot of the available supply voltage from the energy harvester circuit for different input voltage level.

device interaction. A 1-mH OFF-chip inductor with Q equal to 55 and SRF at 1.8 MHz is placed in series between the powering port and the positive electrode of the HUB device. An inductor with higher Q increases peak power delivery shortening the charging time. Fig. 14(a) shows 4-V peak-to-peak transmitted voltage with 0.4-V supply voltage at 1.06-MHz resonance frequency. The channel bandwidth is found to be 400 kHz at resonance. The transmitted voltage is even higher and reaches beyond 10 V with 1.2-V supply voltage at the same resonance frequency. Fig. 14(b) shows the measured results of the HUB transmitted power. The peak transmitted power at resonance is 130 μW and 650 μW at 0.4- and 1.2-V supply voltage, respectively. Fig. 14(c) shows the available received power and overall power transfer efficiency at the NODE. The transferred power is measured on three different human subjects. We found 240 μW (R_L = 1 kΩ) measured received power on average with 37% efficiency at the NODE. The efficiency remains flat throughout the supply voltage range. During the machine–machine interaction due to the absence of return path capacitance (C_{ret}), the power transfer profile becomes independent of human body parameters.

Fig. 14(d) shows the peak received power in tabletop scenario on three different human subjects at different supply voltages. At 1.2-V supply voltage, the peak received power is in the range of 28 μW–30 μW (R_L = 20 kΩ) with 3% efficiency. During the tabletop interaction, the return path capacitances (C_{ret}) are in the range of 100–200 pF which significantly reduces the transmitted power, hence the received power and efficiency. Similarly in a complete wearable-wearable scenario, the measured transferred power is 5 μW (R_L = 80 kΩ) with 7% efficiency. In the wearable–wearable scenario, the return path capacitances are in the range of 0.5–1 pF which reduces the power loss within the body and turns out to have the overall power transfer efficiency better than tabletop scenario. Fig. 14(e) shows a comparative bar plot of power transfer for different HBC scenarios. In all the three cases, series resonance at the transmitter side increases the received power and transfer efficiency compared to the EQS power transmission due to the increase in peak power transfer at the transmitter side.

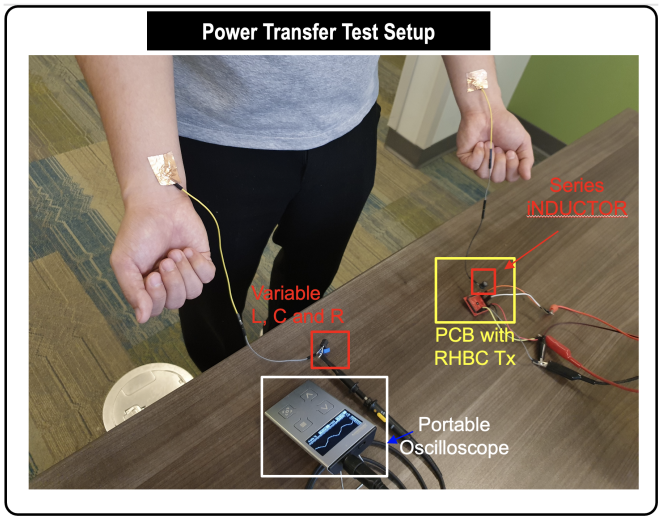

Fig. 16. Demonstration of power transfer using EQS resonant HBC showing the series inductor at the HUB transmitter side and a variable L-C-R circuit with a portable oscillator for voltage measurement at the receiver side.

B. Data Transfer

Unlike power transfer, data transfer between the HUB and NODE is done using parallel resonance at the transmitter side. Another 1-mH inductor is used in parallel connection with one end connected to the signal port of the HUB and the other end to the floating ground electrode. The measurement result shows the transmitter consumes only 2.19-μW power during data communication at the resonance frequency (∼1 MHz) while driving a 30-pF load at 20-kbps data rate [Fig. 14(f)]. This is 33% lower than EQS-HBC due to the cancellation of the parallel plate capacitor C_P. The HUB control unit and the digitally controlled starved oscillator consume 0.3-μW average power. Fig. 15(a) shows the receiver operates at 10^{-5}

TABLE I
COMPARISON WITH STATE OF THE ART

Comparison Table with State-of-the-Art HBC Transceivers and Energy Harvesting Techniques for Wearables

	Powering & Comm	Only Powering				Only Communication			
	This Work	**J. Li ISSCC '20**	**I. Park ISSCC '18**	**M. Meng ISSCC '19**	**L. Xia JSSC '14**	**S. Maity CICC '19**	**H. Cho ISSCC '15**	**J. Park ISSCC '19**	**J. Lee ISSCC '14**
Technique	Resonant EQS (Body Coupled)	Body-coupled + Ambient	Tribo Electric Harvesting	Piezo-electric Harveting	Far Field RF Harvesting	Capacitive	Capacitive	Magnetic	Capacitive
Process	65nm CMOS	40nm CMOS	180nm BCD	0.35um CMOS	65nm CMOS	65nm CMOS	65nm CMOS	65nm CMOS	65nm CMOS
Operating Freq	0.5-2 MHz	40 MHz Tx 50/60 Hz	100 Hz	90-160 Hz	904.5 MHz	0.1-1 MHz	10/13.56 MHz	40 MHz	40-80 MHz
Human Body Powering	**Yes**	**Yes**	No	No	No				
Power Delivered	240 uW (Machine-Machine) **28 uW** (Tabletop), Whole Body 5uW (Wearable-Wearable)	**1 uW** (100cm, Tabletop) 100 uW (~cm)	2-8 uW	2-13 uW	231.6 uW(<3m)				
Transmit Power	**650 uW** (Max) → **Safer**	**3mW**	NA	NA	20 dBm				
Efficiency	37%(Machine-Machine) **3%**(Tabletop) 7% (Wearable-Wearable)	**0.03**-3.33%	NA	NA	0.232%				
Coverage	Full Body (Distance **Independent**)	Full body (Distance **Dependent**)	Joint and feet	Limbs	0.9-9m (antenna dependent)				
Modulation	OOK					OOK	OOK	OOK	Walsh Coding
Supply Voltage	0.5					0.5	0.8	0.6	1.1
Data Rate	1-20Kbps					1-20Kbps	100Kbps	5 Mbps	60 Mbps
Tx Power	1.3uW (10p load) 1.5uW (20p load) **2.19uW (30p load)**					**3.7 uW** @1MHz f_c (30p load)	21 uW	35.8uW	1.85mW
Rx Power	**72nW** (with on-chip OSC and CDR)					**1.4 uW**	42.5 uW	24uW	9.02mW
Sensitivity	-60 dBm @10^{-5} BER					-64dBm @10^{-3} BER	-60 dBm @10^{-5} BER	-56 dBm @10^{-3} BER	-58 dBm @<10^{-5} BER

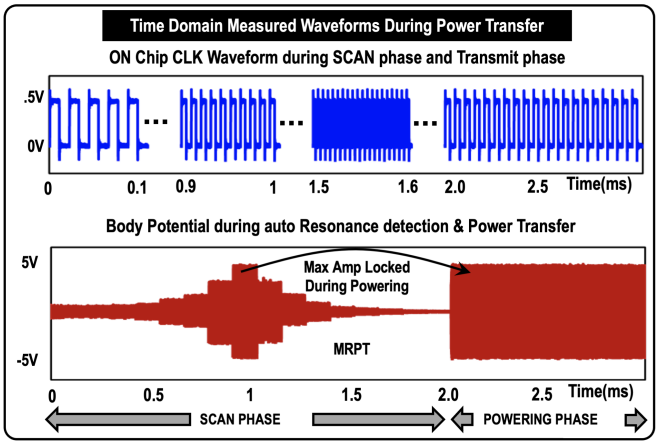

Fig. 17. Captured time-domain waveforms showing the ON-chip clock output and the body potential during power transfer using series resonance. The first 2 ms is used for frequency scanning and resonance detection followed by power transmission at the end of the scanning phase.

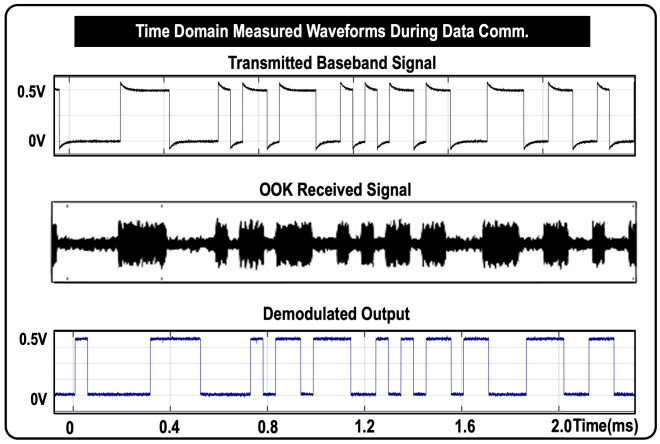

Fig. 18. Captured time-domain waveforms showing the transmitted baseband signal, received OOK data, and demodulated output of the receiver.

BER at 20-kbps data rate with a 0.56 UI timing margin. The receiver shows a sensitivity of −60 dBm (318 μV) and −52 dBm (794 μV) with 1- and 20-kbps data rates, respectively [Fig. 15(b)]. At the lowest power mode, the receiver consumes only 72-nW power. The response of the energy harvester in the NODE device is shown in Fig. 15(c).

Area and Power Breakdown

		Blocks	Area (μm^2)	Standby Power @20kbps (uW)	Active Power @20kbps (uW)	% Leakage Power	Total Active Power(uW)
Power Transfer	Power Tx	CLK Gen+Control	36800	0.1	0.2	33.3	650.2
		Power Buffer	1000	7	650 (During P_{TX})	1.1	
	Harvester	Rectifier+VR	33200	NA	NA	NA	NA
Data Comm.	Data Tx	CLK Gen	16000	0.1	0.2	33.3	2.19
		PRBS Gen+ Buffer	5000	0.26	1.99 (30p load)	11.5	
	Data Rx	Analog Front End	18000	0.042	0.04	51.2	0.072
		CDR+CLK Gen	17000	0.08	0.032	71	

Chip Micrograph

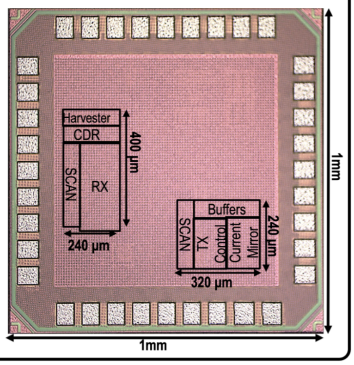

Fig. 19. Block level area and power breakdown of the EQS resonant HBC IC in different operating modes with chip micrograph on the right side.

C. Demonstration: Power and Data Transfer

The demonstration of power transfer from a HUB device to NODE in tabletop condition using EQS resonant HBC is shown in Fig. 16. The battery-operated HUB device injects power through the left arm. An OFF-chip inductor is placed in series at the transmitter side. On the receiving side (right-hand), an L-C-R circuit with variable capacitance and resistance is used to do the maximum power transfer with impedance matching. A portable oscillator is used to measure the voltage across the resistance. Stretching the arm or changing the posture indeed has some effect on the channel loss. However, the variation of channel loss across nominal postures of the hand shows 8-dB variation even across different environments. These variations result primarily from the changes in return path capacitance and body shadowing [22]. However, with our automatic resonance frequency tracking loop, we would be able to nullify some of these changes, originating from the return path capacitance variation, by changing the frequency of transmission and hence even have less effect of variation.

The time-domain measured waveform during the power transfer from HBC HUB to NODE is shown in Fig. 17. The initial 2 ms is used for scanning and detection of the resonance frequency. At the end of the scanning phase, the frequency is locked at resonance and the transmission phase begins. The signal waveforms during data communication are shown in Fig. 18. The signal is sent at a 20-kbps data rate with a carrier frequency set at resonance (∼1 MHz).

D. Power Breakdown

Fig. 19 shows the area and power breakdown of the proposed design along with the chip micrograph to the right. The power transmitter can operate at the maximum possible supply of 1.2 V to transmit 650 μW of peak power into the body. Almost 99.9% power is consumed in the driving buffer to send the power to the body. The driving buffer has 1.1% leakage power. The total power consumption of the power transmitter including the clock generation unit and control circuitry is 650.2 μW. The receiver can operate at a 0.4–0.8-V supply range. It is not possible to operate at a 20-kbps data rate with tolerable sensitivity at supply voltages below 0.6 V. Operating at a 20-kbps data rate with the lowest power mode requires 2.19 μW in data transmitter and 72 nW in data receiver.

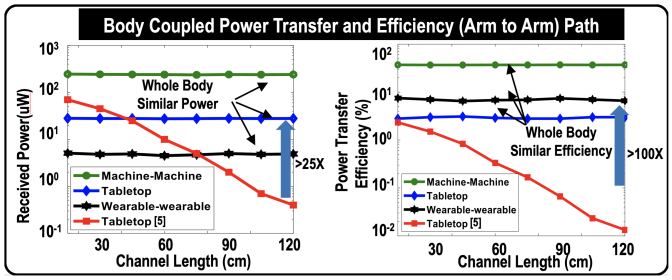

Fig. 20. Received power and power transfer efficiency with respect to channel length in three different HBC scenarios, showing 25× and 100× improvement, respectively, over the state of the arts [6].

E. Comparison

Table I shows the comparison of this work with other state-of-the-art implementations. The comparison table is divided into two groups: 1) for powering and 2) for communication, as the proposed design is capable of delivering power and data both depending on the requirement. The HBC HUB can operate at a variable frequency range of 0.5–2 MHz and can transmit power 650 μW which is also within the safer limit of power level set by [19], [20]. In the wearable–wearable whole body power transfer scenario for the long channel, the achieved efficiency is 7%, making this EQS resonant power transfer more than 100× efficient compared to the previous state of the work which is based on body-coupled and ambient powering principle [5]. The proposed work and [5] are suitable for human body powering, whereas this work outperforms [5] in power delivery and efficiency for long channel as shown in Fig. 20.

V. Conclusion

This article presents the first thorough theoretical development of the EQS resonant HBC bio-physical model, transfer function equations, and FoM for communication. It describes the advantage of series resonance which provides Q^4 times

benefit in peak power transfer over regular EQS HBC. Similarly, parallel resonance provides Q^3 times benefit in FoM during DATA communication over regular EQS HBC. This is the first μW solution for channel-independent wearable–wearable whole-body power transfer. Series resonance with a powerful driver injects high power into the body using inductive cancellation and EQS operation provides channel-independent whole-body powering. An MRPT loop is used to track the resonance frequency which ensures real-time maximum peak power transfer from battery-operated HUB device to the energy-harvested NODE. The peak received power in machine–machine, tabletop, and wearable–wearable scenario is 240 μW with 37% efficiency, 28 μW with 3% efficiency, and 5 μW with 7% efficiency, respectively. This is a 100$\times$ improvement in the body coupled power transfer efficiency and more than 10$\times$ improvement in peak power transfer for long channel compared to the state of the art. This article also demonstrates the first 2.19 μW DATA communication TRx at 20-kbps data rate while driving 30-pF plate-to-plate device capacitance. Due to the inductive cancellation, the power budget for data communication is 33% lower than the power budget of EQS HBC while driving the same capacitive load. This article includes an ON-chip clock generator for variable-frequency operation in HBC HUB and energy-harvested powering of the HBC NODE, making the battery-less perpetual mobile operation a reality.

REFERENCES

[1] S. Maity, M. He, M. Nath, D. Das, B. Chatterjee, and S. Sen, "Bio-physical modeling, characterization, and optimization of electro-quasistatic human body communication," *IEEE Trans. Biomed. Eng.*, vol. 66, no. 6, pp. 1791–1802, Jun. 2019.

[2] S. Maity, D. Yang, S. S. Redford, D. Das, B. Chatterjee, and S. Sen, "BodyWire-HCI: Enabling new interaction modalities by communicating strictly during touch using electro-quasistatic human body communication," *ACM Trans. Computer-Human Interact.*, vol. 27, no. 6, pp. 1–25, Dec. 2020, doi: 10.1145/3406238.

[3] J. Lee *et al.*, "30.7 A 60 Mb/s wideband BCC transceiver with 150 pJ/b RX and 31 pJ/b TX for emerging wearable applications," in *IEEE ISSCC Dig. Tech. Papers*, Feb. 2014, pp. 498–499.

[4] S. Maity *et al.*, "Sub-uwrcomm 415-nw 1-10-kbps physically and mathematically secure electro-quasi-static HBC node for authentication and medical applications," *IEEE J. Solid-State Circuits*, vol. 56, no. 3, pp. 788–802, Mar. 2021.

[5] J. Li *et al.*, "Human-body-coupled power-delivery and ambient-energy-harvesting ICs for a full-body-area power sustainability," in *IEEE ISSCC Dig. Tech. Papers*, Feb. 2020, pp. 514–516.

[6] J. Li, Y. Dong, J. H. Park, and J. Yoo, "Body-coupled power transmission and energy harvesting," *Nature Electron.*, vol. 4, no. 7, pp. 530–538, Jul. 2021. [Online]. Available: https://www.nature.com/articles/s41928-021-00592-y

[7] J. Yoo, S. Lee, and H.-J. Yoo, "A 1.12 pJ/b inductive transceiver with a fault-tolerant network switch for multi-layer wearable body area network applications," *IEEE J. Solid-State Circuits*, vol. 44, no. 11, pp. 2999–3010, Nov. 2009.

[8] J. Yoo, L. Yan, S. Lee, Y. Kim, and H.-J. Yoo, "A 5.2 mW self-configured wearable body sensor network controller and a 12 μ W wirelessly powered sensor for a continuous health monitoring system," *IEEE J. Solid-State Circuits*, vol. 45, no. 1, pp. 178–188, Jan. 2010.

[9] N. Desai, J. Yoo, and A. P. Chandrakasan, "A scalable, 2.9 mW, 1 Mb/s e-Textiles body area network transceiver with remotely-powered nodes and bi-directional data communication," *IEEE J. Solid-State Circuits*, vol. 49, no. 9, pp. 1995–2004, Sep. 2014.

[10] J. Bae, H. Cho, K. Song, H. Lee, and H.-J. Yoo, "The signal transmission mechanism on the surface of human body for body channel communication," *IEEE Trans. Microw. Theory Techn.*, vol. 60, no. 3, pp. 582–593, Mar. 2012.

[11] A. Fort, C. Desset, J. Ryckaert, P. De Doncker, L. Van Biesen, and S. Donnay, "Ultra wide-band body area channel model," in *Proc. IEEE Int. Conf. Commun. (ICC)*, vol. 4, May 2005, pp. 2840–2844.

[12] P. S. Hall and Y. Hao, "Antennas and propagation for body centric communications," in *Proc. 1st Eur. Conf. Antennas Propag.*, Nov. 2006, pp. 1–7.

[13] Y. Kifle, H.-S. Kim, and J. Yoo, "Human body and head characteristics as a communication medium for body area network," in *Proc. 37th Annu. Int. Conf. IEEE Eng. Med. Biol. Soc. (EMBC)*, Aug. 2015, pp. 1845–1848.

[14] D. Kwon and G. A. Rincon-Mora, "A single-inductor 0.35 μm CMOS energy-investing piezoelectric harvester," *IEEE J. Solid-State Circuits*, vol. 49, no. 10, pp. 2277–2291, Oct. 2014.

[15] I. Park, J. Maeng, M. Shim, J. Jeong, and C. Kim, "A high-voltage dual-input buck converter achieving 52.9% maximum end-to-end efficiency for triboelectric energy-harvesting applications," *IEEE J. Solid-State Circuits*, vol. 55, no. 5, pp. 1324–1336, May 2020.

[16] B. Chatterjee *et al.*, "A 1.15μW 5.54 mm^3 implant with a bidirectional neural sensor and stimulator SoC utilizing bi-phasic quasi-static brain communication achieving 6 kbps-10 Mbps uplink with compressive sensing and RO-PUF based collision avoidance," in *Proc. Symp. VLSI Circuits*, Jun. 2021, pp. 1–2.

[17] P.-H. Chen, C.-S. Wu, and K.-C. Lin, "A 50 nW-to-10 mW output power tri-mode digital buck converter with self-tracking zero current detection for photovoltaic energy harvesting," *IEEE J. Solid-State Circuits*, vol. 51, no. 2, pp. 523–532, Feb. 2016.

[18] K. R. Sadagopan, J. Kang, Y. Ramadass, and A. Natarajan, "A 960 pW co-integrated-antenna wireless energy harvester for WiFi backchannel wireless powering," in *IEEE ISSCC Dig. Tech. Papers*, Feb. 2018, pp. 136–138.

[19] *IEEE Standard for Safety Levels With Respect to Human Exposure to Electromagnetic Fields, 0-3 kHz*, IEEE Standard C95.6-2002, Oct. 2002, p. 1.

[20] *IEEE Standard for Safety Levels with Respect to Human Exposure to Radio Frequency Electromagnetic Fields, 3 kHz to 300 GHz*, IEEE Standard C95.1-2005 (Revision IEEE Standard C95.1-1991), Apr. 2006, pp. 1–238.

[21] M. Nath, S. Maity, and S. Sen, "Toward understanding the return path capacitance in capacitive human body communication," *IEEE Trans. Circuits Syst. II, Exp. Briefs*, vol. 67, no. 10, pp. 1879–1883, Oct. 2020.

[22] A. Datta, M. Nath, D. Yang, and S. Sen, "Advanced biophysical model to capture channel variability for EQS capacitive HBC," *IEEE Trans. Biomed. Eng.*, vol. 68, no. 11, pp. 3435–3446, Nov. 2021.

[23] S. Sen, S. Maity, and D. Das, "The body is the network: To safeguard sensitive data, turn flesh and tissue into a secure wireless channel," *IEEE Spectr.*, vol. 57, no. 12, pp. 44–49, Dec. 2020.

[24] V. Mangal and P. R. Kinget, "Sub-nW wake-up receivers with gate-biased self-mixers and time-encoded signal processing," *IEEE J. Solid-State Circuits*, vol. 54, no. 12, pp. 3513–3524, Dec. 2019.

[25] A. Roy Chowdhury, S. Maity, and S. Sen, "Theoretical analysis of multi integrating RX front-ends for lossy broad-band channels," *IEEE Open J. Circuits Syst.*, vol. 2, pp. 363–379, 2021.

[26] S. Oh, N. E. Roberts, and D. D. Wentzloff, "A 116 nW multi-band wake-up receiver with 31-bit correlator and interference rejection," in *Proc. IEEE Custom Integr. Circuits Conf.*, Sep. 2013, pp. 1–4.

[27] V. Mangal and P. R. Kinget, "28.1 A 0.42 nW 434 MHz -79.1 dBm wake-up receiver with a time-domain integrator," in *IEEE ISSCC Dig. Tech. Papers*, Feb. 2019, pp. 438–440.

Nirmoy Modak (Student Member, IEEE) received the B.E. degree in electronics and telecommunication engineering from Jadavpur University, Kolkata, India, in 2012, and the M.Tech. degree in electrical engineering from IIT Bombay, Mumbai, India, in 2015. He is currently pursuing the Ph.D. degree in electrical engineering with Purdue University, West Lafayette, IN, USA.

He was an Electrical Design Engineer with Cypress Semiconductor Pvt. Ltd., Bengaluru, India, from 2015 to 2016. He is currently an Assistant Professor with the Electronics and Telecommunication Department, Jadavpur University. His research interests include mixed-signal circuit design and low power system design for human body communication.

Mr. Modak was a recipient of the IEEE CICC Best Student Paper Award in 2021.

Debayan Das (Member, IEEE) received the bachelor's degree in electronics and telecommunication engineering from Jadavpur University, Kolkata, India, in 2015, and the Ph.D. degree in electrical and computer engineering from Purdue University, West Lafayette, IN, USA, in 2021.

He worked as an Analog Design Engineer at a startup based in India. He has interned with the Security Research Lab, Intel Labs, Hillsboro, OR, USA, over the summers of 2018 and 2020. He is currently working as a Security Researcher with Intel Corporation. His research interests include hardware security and mixed-signal IC design.

Dr. Debayan was a recipient of the IEEE HOST Best Student Paper Award in 2017 and 2019, CICC 2021 Best Student Paper Award, the 2nd Best Demo Award in HOST 2020, and the 3rd Best Poster Award in IEEE HOST 2018. In 2019, one of his papers was recognized as a Top Pick in Hardware and Embedded Security published over the span of 6 years. He was recognized as the winner (third place) of the ACM ICCAD 2020 Student Research Competition (SRC). During his Ph.D. degree, he has been awarded the ECE Fellowship from 2016 to 2018, the SSCS Pre-doctoral Achievement Award in 2020-2021, the Bilsland Dissertation Fellowship from 2020 to 2021, and the Outstanding Graduate Student Research Award by the College of Engineering, Purdue University.

Mayukh Nath (Graduate Student Member, IEEE) received the B.S. degree in physics from the Indian Institute of Science, Bengaluru, India, in 2016. He is currently pursuing the Ph.D. degree in electrical engineering with Purdue University, West Lafayette, IN, USA.

His research interests include electromagnetic theory and simulation-based formulation of inter-device communications, such as body area network-based medical implants and wearables. He is also interested in electromagnetism-based fundamental formulation of side channel attack and prevention techniques.

Baibhab Chatterjee (Member, IEEE) received the B.Tech. degree in electronics and communication engineering from the National Institute of Technology (NIT), Durgapur, India, in 2011, and the M.Tech. degree in electrical engineering from IIT Bombay, Mumbai, India, in 2015. He is currently pursuing the Ph.D. degree with the School of Electrical Engineering, Purdue University, West Lafayette, IN, USA.

His industry experience includes 2 years as a Digital Design Engineer/a Senior Digital Design Engineer with Intel, Bengaluru, India, and 1 year as a Research and Development Engineer with Tejas Networks, Bengaluru. His research interests include low-power analog, RF, and mixed-signal circuit design for secure biomedical applications.

Mr. Chatterjee received the University Gold Medal from NIT, Durgapur, India, in 2011, the Institute Silver Medal from IIT Bombay in 2015, the Andrews Fellowship at Purdue University from 2017 to 2019, the HOST 2018 Best Student Poster Award (3rd), the CICC 2019 Best Paper Award (overall), the RFIC/IMS 2020 3MT Award (audience choice), and the Bilsland Fellowship at Purdue University from 2021 to 2022.

Gaurav Kumar K (Student Member, IEEE) received the bachelor's degree in electronics and telecommunication engineering from Jadavpur University, Kolkata, India, in 2017. He is currently pursuing a Ph.D. degree in electrical and computer engineering with Purdue University, West Lafayette, IN, USA, working with Prof. S. Sen.

His research interests include mixed-signal IC design for low-power and high-speed sensors.

Shovan Maity (Member, IEEE) received the B.E. degree from Jadavpur University, Kolkata, India, in 2012, the M.Tech. degree in electrical engineering from IIT Bombay, Mumbai, India, in 2014, and the Ph.D. degree in electrical engineering from Purdue University, West Lafayette, IN, USA, in 2019.

He worked as an Analog Design Engineer with Intel, Bengaluru, India, from 2014 to 2016 and a Senior Circuit Design Engineer with Qualcomm, San Diego, CA, USA from 2019 to 2021. He is currently working as a Staff Research Scientist in a Stealth Mode startup. His research interests lie in the area of mixed-signal circuits and systems for the Internet of Things, and biomedical and security applications.

Dr. Maity received the Institute Silver Medal from IIT Bombay in 2014, the Purdue ECE Fellowship from 2018 to 2019, the IEEE HOST Best Student Paper Award in 2017, and the CICC 2019 Best Paper Award.

Shreyas Sen (Senior Member, IEEE) received the Ph.D. degree in ECE from Georgia Tech, Atlanta, GA, USA, in 2011.

He is currently an Associate Professor in ECE with Purdue University. He has over 5 years of industry research experience with Intel Labs, Hillsboro, OR, USA, Qualcomm, Austin, TX, USA, and Rambus, Los Altos, CA, USA. He is the Inventor of the Electro-Quasistatic Human Body Communication, for which, he is the recipient of the MIT Technology Review top-10 Indian Inventor Worldwide under 35 (MIT TR35 India) Award. His work has been covered by 100+ news releases worldwide, invited appearance on TEDx Indianapolis, Indian National Television CNBC TV18 Young Turks Program and NPR subsidiary Lakeshore Public Radio. He has coauthored two book chapters, over 135 journal and conference papers, and has 14 patents granted/pending. His current research interests span mixed-signal circuits/systems and electromagnetics for the Internet of Things (IoT), biomedical, and security.

Dr. Sen is a recipient of the NSF CAREER Award 2020, the AFOSR Young Investigator Award 2016, NSF CISE CRII Award 2017, the Google Faculty Research Award 2017, the Intel Labs Quality Award for industry wide impact on USB-C type, the Intel Ph.D. Fellowship 2010, the IEEE Microwave Fellowship 2008, and seven best paper awards including IEEE CICC 2019 and IEEE HOST in 2017, 2018, and 2019. His work was chosen as one of the top-10 papers in the Hardware Security field over the past 6 years (TopPicks 2019). He serves/has served as an Associate Editor for the IEEE Design and Test, Executive Committee member of the IEEE Central Indiana Section and Technical Program Committee member of DAC, CICC, DATE, ISLPED, ICCAD, ITC, VLSI Design, among others.